A Wideband Reconfigurable Intelligent Surface for 5G Millimeter-Wave Applications

Ruiqi Wang, Yiming Yang, *Graduate Student Member, IEEE*, Behrooz Makki, *Senior Member, IEEE*, and Atif Shamim, *Fellow, IEEE*

***Abstract*— Despite the growing interest in reconfigurable intelligent surfaces (RISs) for millimeter-wave (mm-wave) bands, and the considerable theoretical work reported by the communication community, there is a limited number of published works demonstrating practical implementations and experimental results. To the authors' knowledge, no published literature has reported experimental results for RISs covering the n257 and n258 mm-wave bands. In this work, we propose a novel wideband RIS design that covers the entire mm-wave 5G n257 and n258 bands. In simulations, the unit cell can maintain a phase difference of 180° ± 20° and a reflection magnitude greater than −2.8 dB within 22.7 to 30.5 GHz (29.3% bandwidth) using 1-bit p-i-n switches. The proposed unit cell design with four circular cutouts and long vias could realize wideband performance by exciting two adjacent high-order resonances (2.5 and 3.5 f). The periodic unit cells can maintain an angular stability of ±30°. Based on the proposed unit cell, a 20 × 20 RIS array is designed and fabricated with a size of 7.1λ × 7.1λ. The measurement results demonstrate that the proposed RIS could maintain a 3 dB peak gain variation bandwidth among various array configurations within 22.5 to 29.5 GHz (26.9%) and with a beam scanning capability of 50°, making this design a good candidate for 5G mm-wave applications.**

***Index Terms*— Beam scanning, fifth generation (5G), mm-wave, reconfigurable intelligent surface (RIS), wideband.**

I. Introduction

RECENTLY, fifth-generation (5G) millimeter-wave (mm-wave) communication systems have received significant commercial and research attention due to their sizeable available bandwidth [1], [2], [3], [4], [5]. Although the 5G mm-wave system could significantly improve the data rate and communication capacity, the electromagnetic (EM) wave propagation suffers from a higher atmospheric attenuation. Thus, at such frequencies, the EM waves can get severely affected or even blocked by obstacles, causing signal blind spots and restricting the system to line of sight (LOS) communication. Such a problem is even more visible beyond the 5G network with increased quality-of-service requirements and higher frequencies. A reconfigurable intelligent surface (RIS) is beneficial to solve this problem because it can help establish a secondary LOS to maintain the communication link when a blockage occurs in the direct path between the transmitter (Tx) and receiver (Rx) [6]. A conceptual scheme of the RIS in a practical urban environment with multiple signal blind spots is depicted in Fig. 1, where the RIS is able to provide a second LOS to address the blind spots. This RIS-based wireless communication is controllable and programmable, which means that there can be unprecedented opportunities for improving the quality of service for wireless communication systems [6].

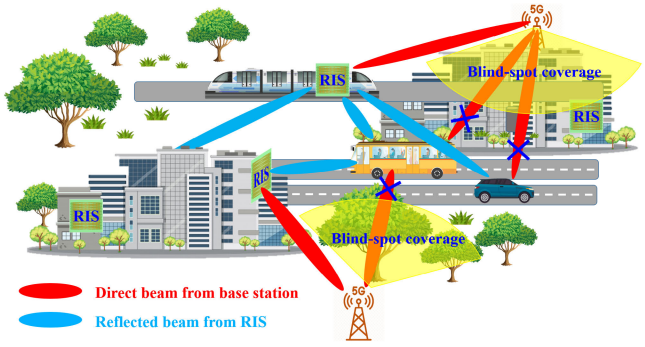

Fig. 1. Conceptual scheme of the RIS in practical applications.

Despite the great performance enhancement promise of RISs, there is not much experimental evidence in the published literature that supports these claims. Most published works focus on the ideal RIS and are limited to theoretical analyses. For example, [7] reported an ideal and theoretical RIS for energy-efficient downlink multiuser communication applications. Similarly, [8] proposed the concept of RIS-assisted communications on the realm of index modulation. In addition, [9] and [10] reported on optimization methods for RIS beamforming for wireless network designs.

However, published literature related to practical RIS designs and their experimental characterization, particularly for mm-wave bands, is scarce. Out of the experimental studies, the majority have been conducted on the sub-6 GHz band [11], [12], [13], [14], and some operate at around 10 GHz [15], [16]. Few reports have addressed practical

Manuscript received 22 April 2023; revised 30 November 2023; accepted 1 January 2024. Date of publication 18 January 2024; date of current version 7 March 2024. This work was supported by Ericsson Research under Grant OSR#4606. *(Corresponding author: Ruiqi Wang.)*

Ruiqi Wang, Yiming Yang, and Atif Shamim are with the Computer, Electrical and Mathematical Sciences and Engineering Division, King Abdullah University of Science and Technology (KAUST), Thuwal 23955, Saudi Arabia (e-mail: ruiqi.wang.1@kaust.edu.sa; yiming.yang@kaust.edu.sa; atif.shamim@kaust.edu.sa).

Behrooz Makki is with Ericsson Research, Ericsson, 417 56 Gothenburg, Sweden (e-mail: behrooz.makki@ericsson.com).

Color versions of one or more figures in this article are available at https://doi.org/10.1109/TAP.2024.3352828.

Digital Object Identifier 10.1109/TAP.2024.3352828

RIS designs operating at mm-wave bands. For example, Gros et al. [17] proposed a practical RIS design and performed near- and far-field measurements for signal enhancement. However, the working bandwidth for the design [17] is from 27.5 to 29.5 GHz (7% bandwidth), which cannot fulfill the large bandwidth requirements for 5G mm-waveband. Shekhawat et al. [18], [19] designed a compact unit cell and a 25 × 32-element RIS prototype working at 28.5 GHz, but the operation bandwidth was not provided. Rains et al. [20] proposed a unit cell design based on varactors. However, the results were obtained from a simulation, and no experimental results were demonstrated. Moreover, the bandwidth is still narrow, so the unit cell phase shift within the 180° ± 20° can be maintained between 24.7 and 26.6 GHz (7.5%). The 5G mm-wave frequency bands contain n257 (26.5 to 29.5 GHz), n258 (24.25 to 27.5 GHz), n259 (39.5 to 43.5 GHz), n260 (37 to 40 GHz), and n261 (27.5 to 28.35 GHz) bands. Therefore, the designed RIS for the n257 and n258 bands (n261 is within the n257 band) needs to cover the bandwidth from 24.25 to 29.5 GHz (19.5%), which is challenging and there is no previously reported work that has realized wideband p-i-n-switch-based RIS to cover this 5G mm-waveband (24.25 to 29.5 GHz).

In this work, we designed, fabricated, and tested a novel 5G mm-wave RIS. A novel unit cell design of patches with four circular cutouts is proposed to satisfy the sizeable bandwidth requirements for the 5G mm-waveband. The proposed unit cell demonstrates wideband performance by exciting two adjacent high-order resonant modes (2.5 and 3.5 f) with the help of four circular cutouts on the edge of the patch element, fully covering the 5G mm-wave n257 and n258 bands (24.25 to 29.5 GHz). The design maintains a simple structure with three layers (patch, ground, and biasing network layers). The p-i-n switches are designed on the backside of the RIS, avoiding interference from diodes and soldering pads. The designed unit cell structure provides adequate space for biasing line routing. A final 20 × 20 array with a size of 7.1λ × 7.1λ is characterized using a two-horn measurement setup. The result reveals a 3 dB gain bandwidth from 22.5 to 29.5 GHz (26.9%) and a 50° beam-scanning range.

II. Unit Cell Design and Simulation

Generally, the RIS is constructed using an array of unit cell elements with tunable EM resonators, which could modify the reflective waves by controlling the characteristic of each unit cell, such as the resonant frequency, reflection amplitude, phase, and polarization. Meanwhile, the RIS design should be distinguished from reconfigurable reflectarray designs [21], [22], [23], [24] because reflectarrays have a fixed incident feed location and generally work in the near-field region for the feeding source antenna. Thus, reflectarray designs optimize the feed antenna and reflectarray elements to achieve optimum performance. The RIS, however, mainly concentrates on the reconfigurable element design and the surface distribution.

In this work, the structure of the proposed unit cell design is depicted in Fig. 2. The top metallic layer is a square patch whose side length is 3 mm. There are four 1.1 mm radius circular cutouts at its four edges, and the total length

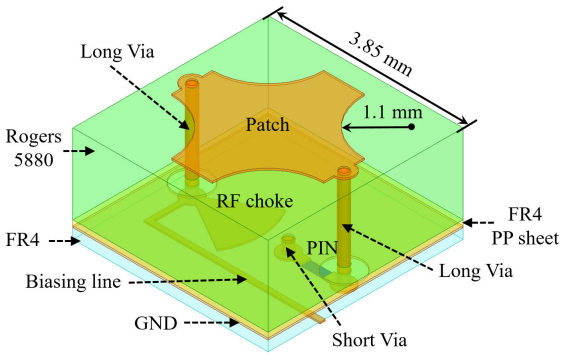

Fig. 2. Proposed unit cell design.

is 3.85 mm. Two side edges of the patch element are connected with vias (0.1 mm radius), which pass through two circular cutouts (0.35 mm radius) on the middle ground to attach the feeding network at the bottom layer. The top substrate is a 1.575 mm Rogers 5880 ($\varepsilon_r = 2.2$, $\tan\delta = 0.0009$) which is low loss and suitable for 5G mm-wave application. Behind the middle ground plane layer is the bottom substrate with a 0.2 mm FR4 ($\varepsilon_r = 4.4$, $\tan\delta = 0.02$) which has less effect on unit cell performance. Two substrate layers are laminated by a 0.1 mm FR4 prepreg sheet ($\varepsilon_r = 4.4$, $\tan\delta = 0.02$). The p-i-n switches are the commercially available type MADP-000907-14020P in MACOM, which displays decent performance in the mm-waveband. One side of the p-i-n switch is connected with the middle ground through a short via, whereas the other side of the switch is connected with the top patch layer by a long via. By adjusting the biasing current, the p-i-n switch could work in two different states, ON and OFF, to achieve reconfigurability. A radio frequency (RF) choke is employed at the end of the long via, ensuring that the unit cell RF performance is not affected by the direct current (dc) feeding lines.

Some innovations of the proposed unit cell design are as follows. First, the proposed unit cell design possesses wideband performance due to the incorporation of circular cutouts into the square patch compared with the traditional square patch. The S_{11} phase performance of the proposed unit cell design and the typical square patch unit cell when the p-i-n switches are in the ON/OFF states is illustrated in Fig. 3. It can be observed that the proposed unit cell with circular cutouts demonstrates steady slope for both of the ON and OFF states [see Fig. 3(a)], whereas the traditional square patch unit cell has a nonuniform phase variation for ON/OFF states [see Fig. 3(b)]. Specifically, the 180° ± 20° phase difference between the ON and OFF states of the proposed unit cell design could be maintained in a wide band from 22.7 to 30.5 GHz (29.3%) and the reflection magnitude is greater than −2.8 dB in this bandwidth, as demonstrated in Fig. 4. The wideband characteristic is attributed to two adjacent resonant modes of 2.5 f (23.1 GHz) and 3.5 f (31.1 GHz) are excited in the ON state. These two adjacent high-order resonances could be moved and optimized, making the 5G mm-wave frequency band located around their middle-frequency range. Meanwhile, adding the circular cutouts can help smooth the surface current and further smooth the resonances.

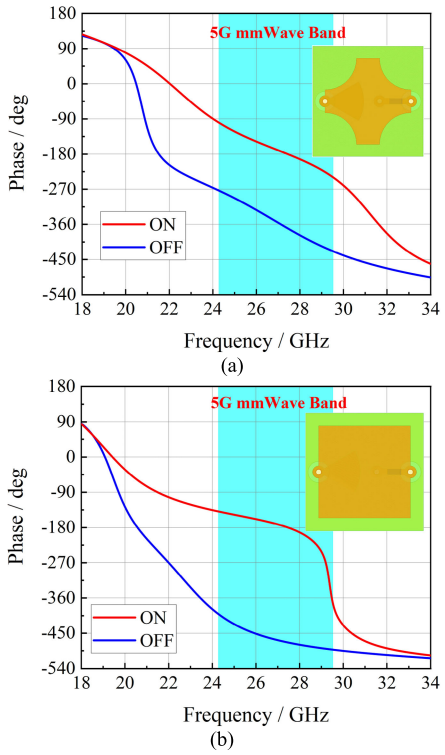

Fig. 3. S_{11} phase of the unit cell element when the p-i-n switch in the ON/OFF states. (a) Proposed unit cell. (b) Traditional square patch unit cell.

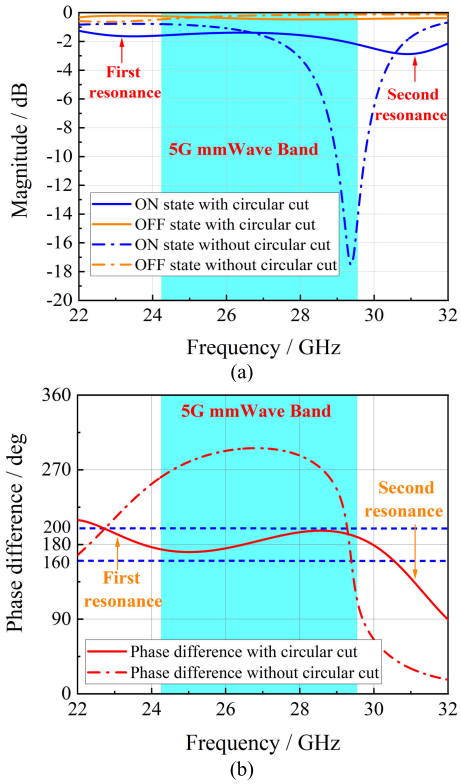

Fig. 4. Performance comparison of the patch unit cell with and without circular cuts. (a) Reflection magnitude. (b) Phase difference.

The detailed surface current distribution of the proposed cell structure is depicted in Fig. 5, where the surface current on the patch element is primarily distributed along the edges of circular cutouts. The dimensions of the circular cuts

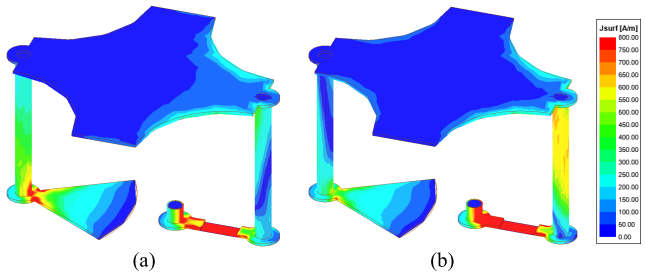

Fig. 5. Surface current distribution of the proposed unit cell in the ON state. (a) 2.5 f (23.1 GHz). (b) 3.5 f (31.1 GHz).

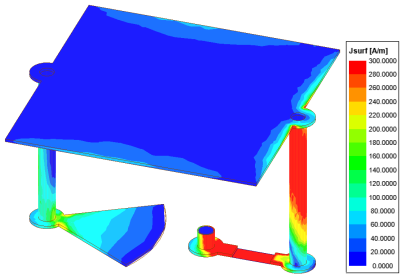

Fig. 6. Surface current of the patch unit cell in the ON state at 3.5 f mode (29.4 GHz).

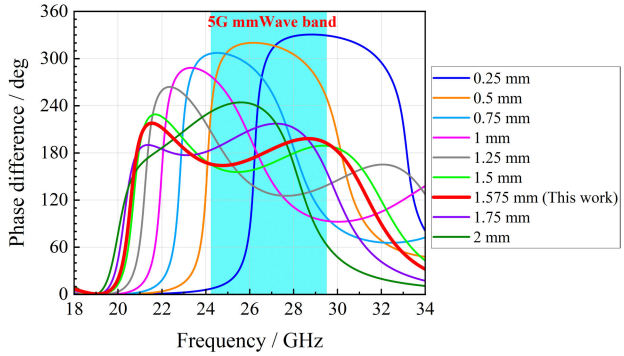

Fig. 7. Phase difference between the ON and OFF states of the proposed unit cell design with various substrate thicknesses.

play critical roles in facilitating the excitation of these two modes. The proposed configuration can be compared with the simulated patch unit cell in Fig. 6, where only one resonant 3.5 f mode occurs in the ON state without the circular cutouts. Therefore, the proposed unit cell has wideband performance generated by exciting two resonant modes through a single layer with a simpler structure. Additionally, the p-i-n diodes are placed at the backside of the middle ground plane to avoid interference with the patch reflection. By placing the radial stubs underneath the resonator with the direction aligned with the p-i-n switches, we can provide space for biasing lines routing between the unit cells to fulfill the compactness requirement. The simple dual-layer stack structure achieves a compact unit cell size of $0.35\lambda \times 0.35\lambda$ (3.85×3.85 mm). On the one hand, a smaller unit cell can effectively avoid the generation of the grating lobes, while, on the other hand, the loss of the unit cell can be effectively reduced by decreasing the lattice size at millimeter wave frequencies [25], [26].

The substrate thickness effect for the proposed unit cell performance has been investigated, as demonstrated in Fig. 7. Specifically, the phase difference between ON and OFF states of

the designed unit cell at normal incidence has been simulated with different substrate thicknesses from 0.25 to 2 mm. It can be observed that a thin substrate, such as 0.25 mm, cannot provide enough phase shift because of the inadequate electrical propagation length difference between these two states [27]. It should be pointed out that the 0.25 mm substrate with 330° phase difference is equivalent to −30°, but ±180° phase differences are demanded for a 1-bit phase quantization RIS. By contrast, a substrate thickness of 1.5–1.75 mm is suitable for the unit cell design with the proposed structure to achieve the required ±180° phase difference within the desired 5G mm-wave bands. Therefore, the RT/duroid 5880 substrate with a standard thickness of 1.575 mm is determined as the final design.

Although the unit cell substrate thickness with 1.575 mm ($0.14\lambda_0$) in this work is already less than or similar to some reported works, such as [27] ($0.16\lambda_0$), [28] ($0.14\lambda_0$), to eliminate the potential influence of the substrate modes due to the thickness of the substrate, the proposed unit cell model (see Fig. 2) without RT/duroid 5880 substrate (i.e., air substrate) has been simulated. The results reveal that the unit cell without RT/duroid 5880 substrate has a broadband operation bandwidth as well, and a phase difference of 180° at around 34 GHz can be observed, where the reflection magnitude for ON and OFF states are −2.5 and −0.4 dB, respectively. These results are almost similar to the unit cell with RT/duroid 5880 substrate (Reflection magnitude: OFF state > −2.8 dB, ON state > −0.5 dB). Meanwhile, as reported in the work [29], by properly choosing the unit cell size, the substrate mode can be greatly reduced. The unit cell size of $0.35\lambda \times 0.35\lambda$ in this work is at the region of lowest power of substrate mode as indicated in [29]. Therefore, it can be concluded that the proposed unit cell design has negligible substrate mode propagation based on the comparison with air substrate, suitable unit cell size, and low substrate permittivity of 2.2.

In practical applications, the incident EM wave direction is arbitrary, requiring the RIS design should have angular stability to deal with incident waves from different directions. The reflection magnitude and phase difference of the proposed design for different incident angles are illustrated in Fig. 8. In the desired 5G mm-waveband (24.25 to 29.5 GHz), the unit cell has a reflection magnitude greater than −2.5 dB, and the phase difference can be maintained from 140° to 200° when incident wave direction varies between 0° and 30°.

III. RIS Design and Simulation

The proposed RIS array is demonstrated in Fig. 9, comprising 400 unit cells (20 × 20). As mentioned above, the designed unit cell structure provides sufficient space for the biasing lines to extend to the board edges. Twenty connectors (DF40TC(3.0)-20DS) were soldered onto the two edges of the printed circuit board (PCB) to connect the biasing lines to the control circuit board behind it. The total array size is 77 × 77 mm, corresponding to $7.1\lambda \times 7.1\lambda$, where λ is the free-space wavelength at the frequency of 27.5 GHz. With additional connectors on the edge of the array, the PCB size is 96 × 96 mm.

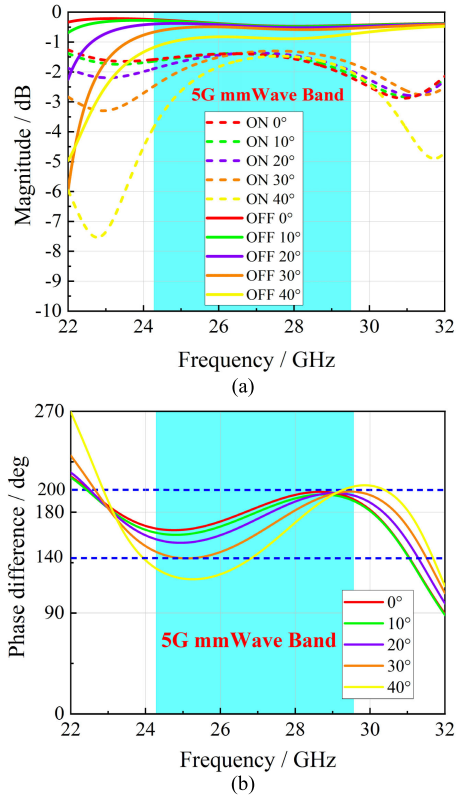

Fig. 8. Angular stability of the proposed unit cell design. (a) Reflection magnitude. (b) Phase difference.

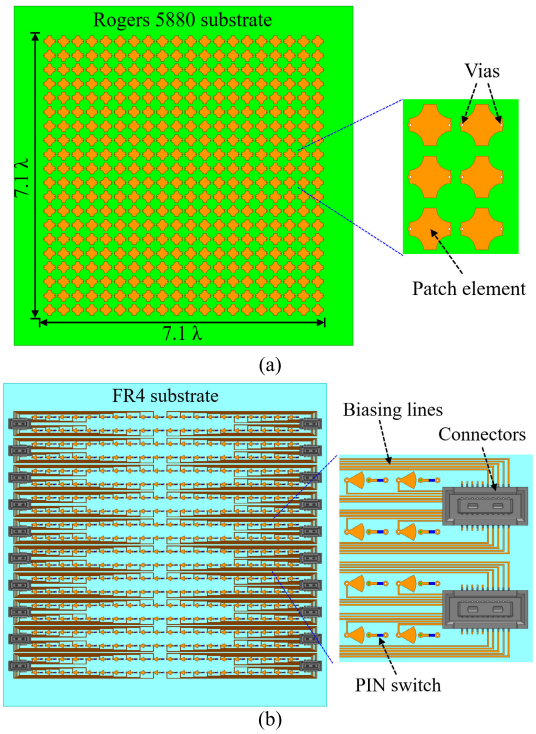

Fig. 9. Array configuration of the proposed RIS. (a) Front view. (b) Back view.

A detailed full-wave simulation model in High-Frequency Simulation Software (HFSS) is depicted in Fig. 10. Each unit element of the proposed RIS is configured based on the discretized phase distribution calculated through the following

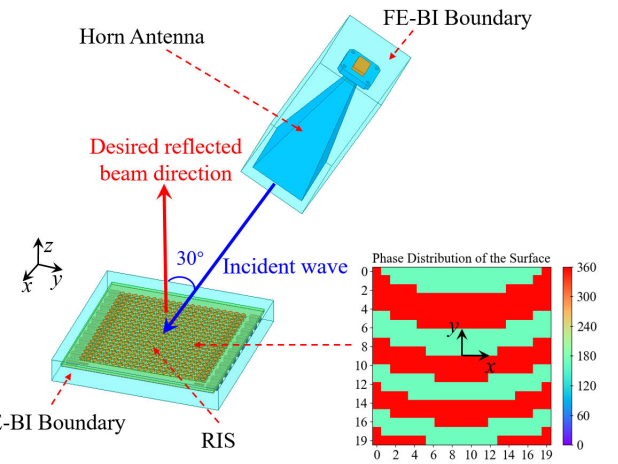

Fig. 10. Full-wave simulation of the proposed RIS.

equation [17]:

$$\varphi_{ij} = k \cdot \left|\vec{r}_{ij}^{\,e} - \vec{r}^{\,f}\right| - k \cdot \left(\vec{u}_0 \cdot \vec{r}_{ij}^{\,e}\right) + \Delta\varphi \tag{1}$$

where φ_{ij} is the ideal phase value for the unit cell at (i, j), $i, j = 1, \ldots, 20$ in this case, k denotes the wavenumber at the free space, r_{ij}^{e} is the element position vector, and r^{f} represents the feed position vector, u_0 indicates the unit vector of the desired reflected beam direction, and $\Delta\varphi$ denotes a constant reference phase. The proposed design has only two states by switching the on and off status of the p-i-n diodes; therefore, the continuous ideal phase distribution should be quantized as two states using the following criterion:

$$\varphi_{ij} = \begin{cases} \varphi_{on}, & \left|\varphi_{ij} - \varphi_{on}\right| \le \left|\varphi_{ij} - \varphi_{off}\right| \\ \varphi_{off}, & \left|\varphi_{ij} - \varphi_{on}\right| > \left|\varphi_{ij} - \varphi_{off}\right| \end{cases} \tag{2}$$

where φ_{on} is the unit cell phase value when the p-i-n switch is on, and φ_{off} is the phase value when the p-i-n is off. These two values can be obtained from the HFSS simulated results of the proposed unit cell. It should be noted that φ_{on} and φ_{off} are frequency dependent, as shown in Fig. 3(a). Thus, the RIS should have a corresponding optimum ON/OFF pattern at a given incident frequency when the other environmental and design parameters are fixed. According to the simulated angular stability of the proposed RIS, it has decent performance with the incident angle varying from $-30°$ to $+30°$. Therefore, in Fig. 10, the incident wave direction is set as $-30°$, transmitted from a WR-34 standard 20 dBi gain horn antenna (PE9851B/SF-20) from 22 to 33 GHz. The phase distribution of the RIS is configured using (1) and (2), with u_0 $(0, 0, 1)$. In the simulation model, the RIS and standard horn are settled in two boxes with finite element boundary integral (FE-BI) to reduce the computational cost of the free space between the horn and the RIS. The simulated 3-D radiation pattern of the proposed RIS at 27.5 GHz is presented in Fig. 11, with a peak gain of 20.9 dBi at 0° reflection, validating the reconfigurability of the designed RIS.

The switch control circuit schematics, control circuit PCB, and flexible printed circuit (FPC) connectors are illustrated in Fig. 12. The RIS array board and control circuits are connected through the FPC. The overall RIS is driven by

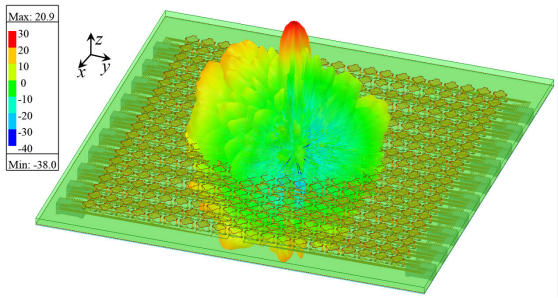

Fig. 11. Three-dimensional radiation pattern of the RIS at 27.5 GHz.

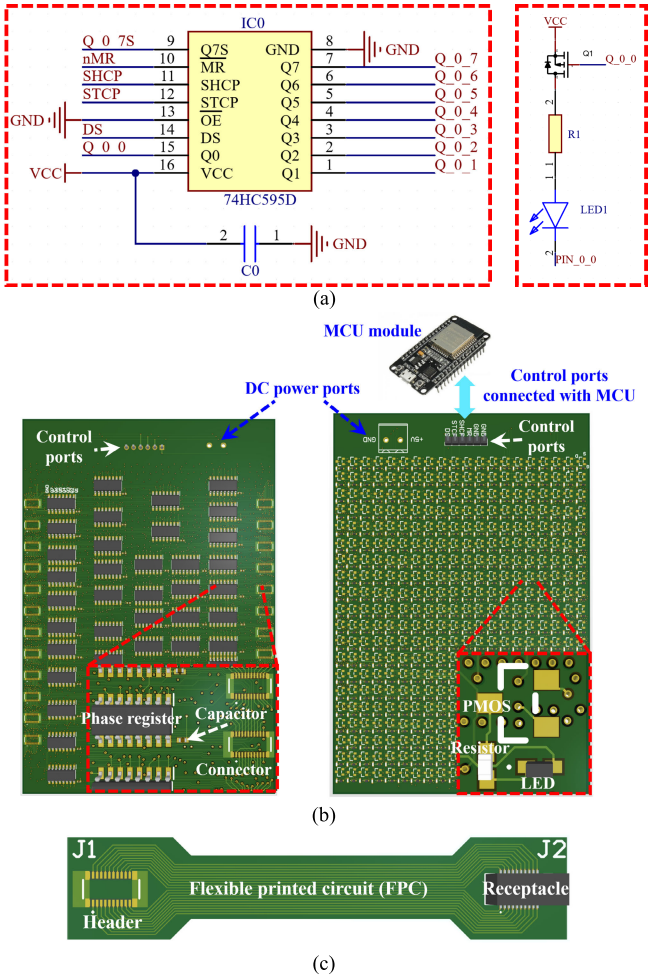

Fig. 12. Control circuit design. (a) Switch control and output schematic. (b) Front and back views of the control board. (c) FPC connectors.

the ESP-WROOM-32 module, which runs a serial communication port for the user interface and computes the array patterns. Attached to the controller are 50 8-bit phase registers (74HC595D), which can multiplex the controller IO and drive the pMOS in order to bias the 400 p-i-n switches. Each p-i-n diode of a unit cell is in series with an LED as a visualization of the p-i-n working state for ease of debugging.

IV. Fabrication and Measurement

The fabricated prototypes of the proposed RIS array configuration, control circuits, and overall RIS design are exhibited in Fig. 13. The components of the designed RIS, including the PCB array, connectors, FPC, and control circuit board

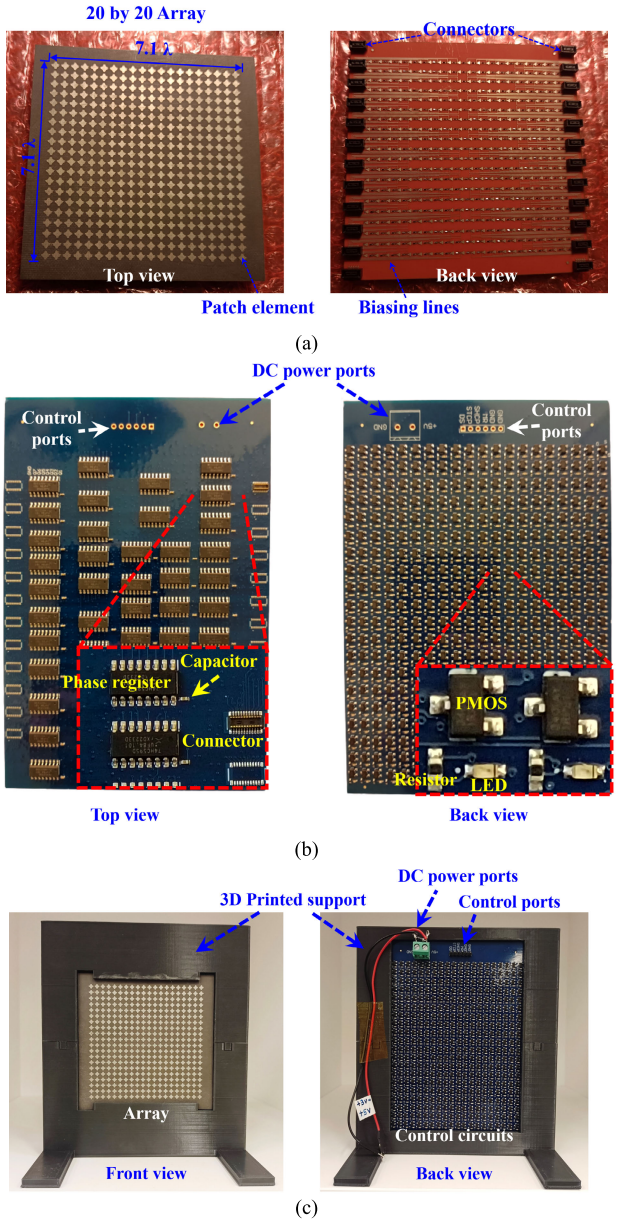

Fig. 13. Fabricated prototype of the proposed RIS design. (a) RIS array. (b) Control circuits. (c) RIS array packaged with control circuits board through FPC connectors.

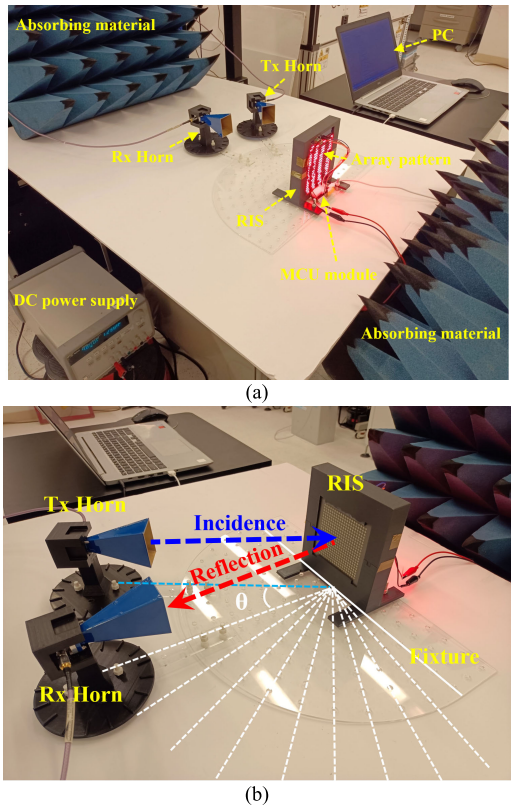

Fig. 14. Practical measurement setup of the proposed RIS design in the near field. (a) Overall measured system. (b) Detailed measured scheme between horns and RIS.

are packaged inside the mechanical supports, which are 3-D-printed using a Raise3D Pro2 printer with polylactic acid filaments. The control circuits are placed at the back side of the package, where the LED arrays demonstrate the ON/OFF state of each unit element. The power supply port contains a positive voltage (+3 to 5 V) and a ground input, which can be connected to a dc power source. Four control ports containing a clock signal, memory reset, and input data are driven by the ESP-WROOM-32 module, which is connected to a computer through USB to receive commands.

The measurement setup of the proposed RIS is depicted in Fig. 14. Two horn antennas (PE9851B/SF-20) are utilized as the Tx and Rx in practical applications, which connect with an Anritsu ME7828A vector network analyzer (VNA). The RIS could reflect the incident beam to the configured beam direction instead of PEC reflection using a specific array pattern. In the measurement process, once the Tx horn position is determined, the RIS will generate the array pattern according to the previously discussed algorithm (1). It should be noted that the array has various patterns depending on the distance between the Tx horn and RIS operation frequency and the desired beam reflection direction. In this measurement, the Tx horn is placed at a distance of 25 cm from the RIS, which works in the near field of the horn antenna. To measure the reflection beam, we move the Rx horn from $-80°$ to $0°$ with a $10°$ step while maintaining the same distance of 35 cm from the RIS. The measured S_{21} parameter between the Tx and Rx horns represents the received signal power level related to the normalized gain of the RIS. Two pieces of absorbing material are placed at the front and back sides of the RIS measurement system to reduce the interference of the behind VNA and surrounding setup. The RIS could reflect the incident beam to the configured beam direction. When the array pattern is off, it has a similar reflected beam as a PEC reflection because all elements have a constant off reflection phase. The comparison between simulation and measurement is demonstrated in Fig. 15, which shows consistency that the measurement agrees well with the simulated results. The discrepancy between simulation and measurement results from the printed support, control circuit, and fabrication and assembly errors of the RIS. It should be noted that the data from $+10°$ to $+50°$ are not measurable because the Tx horn is positioned at $+30°$ that the Rx horn and the Tx horn collide within such angles.

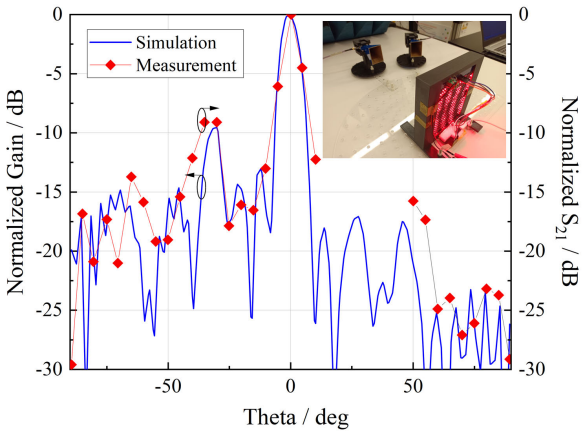

Fig. 15. Comparison between normalized simulated gain and measured S_{21} between Tx and Rx horns.

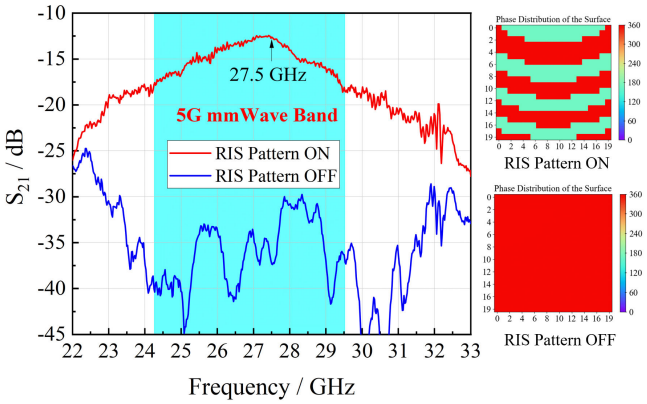

Fig. 16. Measured S_{21} between Tx and Rx horns when turning on/off the RIS pattern in the near field with Tx-RIS distance of 25 cm and RIS-Rx distance of 35 cm.

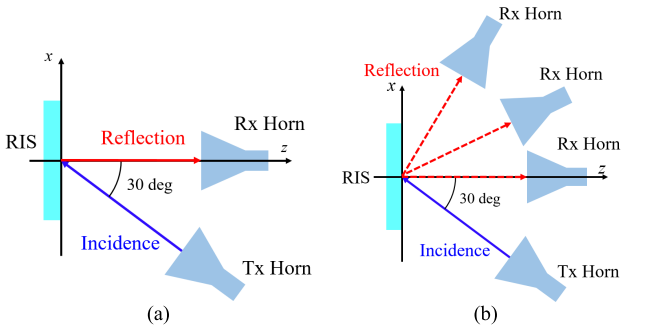

Fig. 17. Measurement scheme. (a) Wideband performance of the proposed RIS. (b) Beam scanning performance of the proposed RIS.

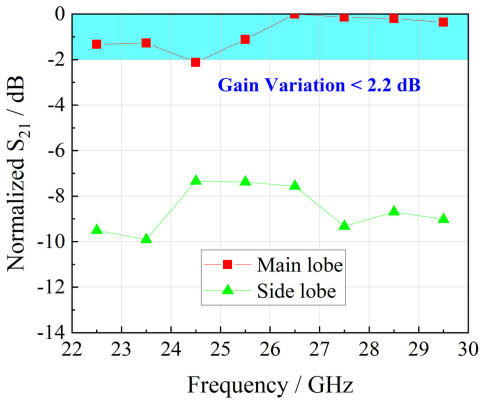

Fig. 18. Measured normalized S_{21} for the main lobes and side lobes at different frequencies.

Moreover, the comparison of the received signal strength level at 0° reflection (30° incidence) between turning on and off the RIS pattern is demonstrated in Fig. 16. A significant improvement from −37.3 to −12.6 dB (24.7 dB enhancement) is observed at the center operation frequency of 27.5 GHz when the RIS pattern turns on compared with the OFF state. An average of 21.2 dB enhancement is obtained for the 5G mm-wave n257 and n258 frequency bands. It should be pointed out that each frequency point has its unique RIS pattern to achieve the optimum reflection performance. The RIS pattern in Fig. 16 is optimized for the 27.5 GHz frequency, where a peak gain is observed over the whole frequency range.

Detailed measurement procedures and results are discussed as follows. First, to validate the practical wideband performance of the proposed RIS design, the same measurements at different frequencies were conducted, as demonstrated in Fig. 17(a). Specifically, the incident wave and desired reflected wave directions were fixed. As discussed in the simulation section, the proposed RIS has angular stability with −30° to 30°. Thus, the Tx horn position is fixed, and the incidence angle is maintained at 30°, whereas the desired reflected beam direction is set to 0°. The measured setup remains the same, but working frequencies changed from 22.5 to 29.5 GHz with a 1 GHz step that each frequency point has a specific array pattern to reflect the 30° incident wave to 0°.

The measured normalized signal strength of the desired beam direction (0° reflection) over a wide frequency range from 22.5 to 29.5 GHz is captured as demonstrated in Fig. 18. Besides RIS, the variation of the measured S_{21} is also due to the variation of both the horn antenna gain and the path loss at different frequencies. To better show the RIS performance itself, we subtract S_{21}_on with S_{21}_off and get the compensated S_{21} of the RIS. It can be observed that the normalized main lobe variation is less than 2.2 dB within the whole measured frequency band. In other words, the proposed RIS design possesses a 3-dB peak gain bandwidth of over 26.9% which can fulfill the 5G mm-wave n257 and n258 bands requirements.

The detailed received signal level comparison of the RIS when array pattern are switched on and off is presented in Fig. 19(a)–(h). The array phase distribution (i.e., ON/OFF state of the p-i-n switches) at different operation frequencies is provided at the upper right corner of each figure. Uniform and consistent results were obtained within the whole frequency band from 22.5 to 29.5 GHz (26.9%), which proves its wideband reconfigurability. The measured sidelobe level (SLL) values for the proposed RIS design are 8.2, 8.7, 5.3, 6.3, 7.6, 9.2, 8.5, and 8.7 dB for frequencies from 22.5 to 29.5 GHz. Therefore, an average of 7.8 dB for the SLL is obtained over the whole frequency range. The reason that the SLL at frequencies around 24.5 and 25.5 GHz is lower than at other frequencies is that the unit cell has a deteriorated phase

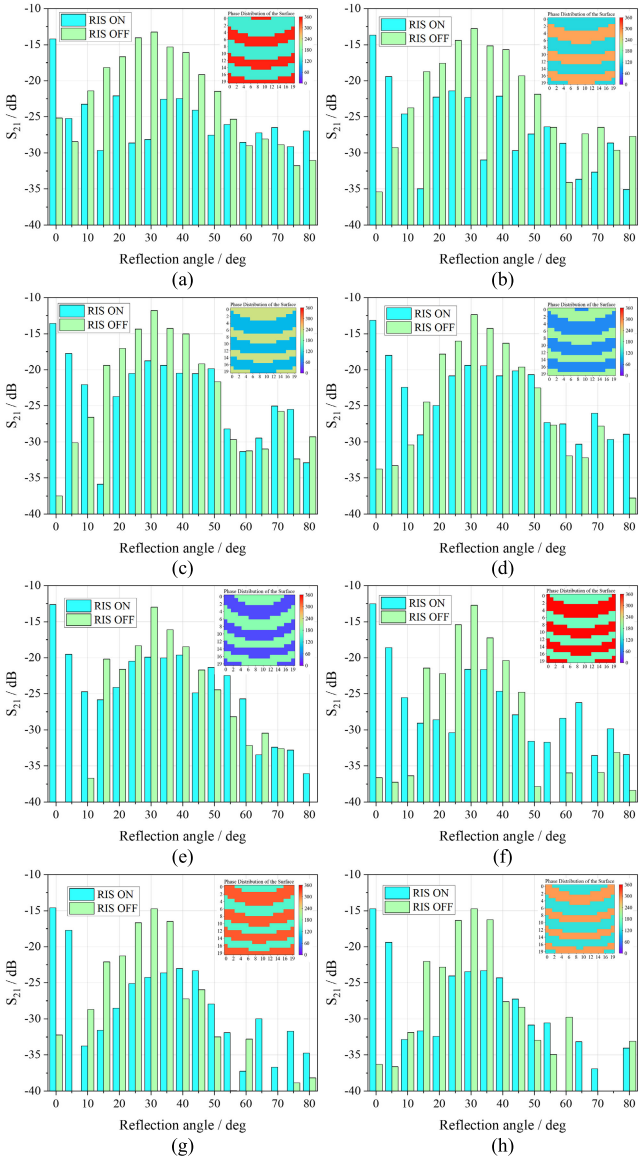

Fig. 19. Measured S_{21} comparison of the RIS reflection when pattern on and off at different frequencies. (a) 22.5 GHz. (b) 23.5 GHz. (c) 24.5 GHz. (d) 25.5 GHz. (e) 26.5 GHz. (f) 27.5 GHz. (g) 28.5 GHz. (h) 29.5 GHz.

difference (140°) at an incident angle of 30° (see Fig. 8). Nevertheless, such a measurement proves that the proposed RIS design has wideband performance that could cover the 5G mm-wave n257 and n258 bands.

Furthermore, another experiment on the beam scanning capability of the proposed design was also conducted. The detailed measured scheme is demonstrated in Fig. 17(b). In this case, the feed source location is the same as the previous experiment with the incident wave direction of 30°. In addition, the operation frequency is fixed at 27.5 GHz. However, this time, the desired beam reflection direction is changed from 0° to 50° to validate the beam scanning performance of the designed RIS. Therefore, the array pattern changes accordingly when with various reflected wave directions.

The measured S_{21} values between the Tx and Rx horns at different reflected beam directions from 0° to 50° are presented in Fig. 20(a)–(f). The maximum reflected beam direction moves from the original 0° to 50° when varying the

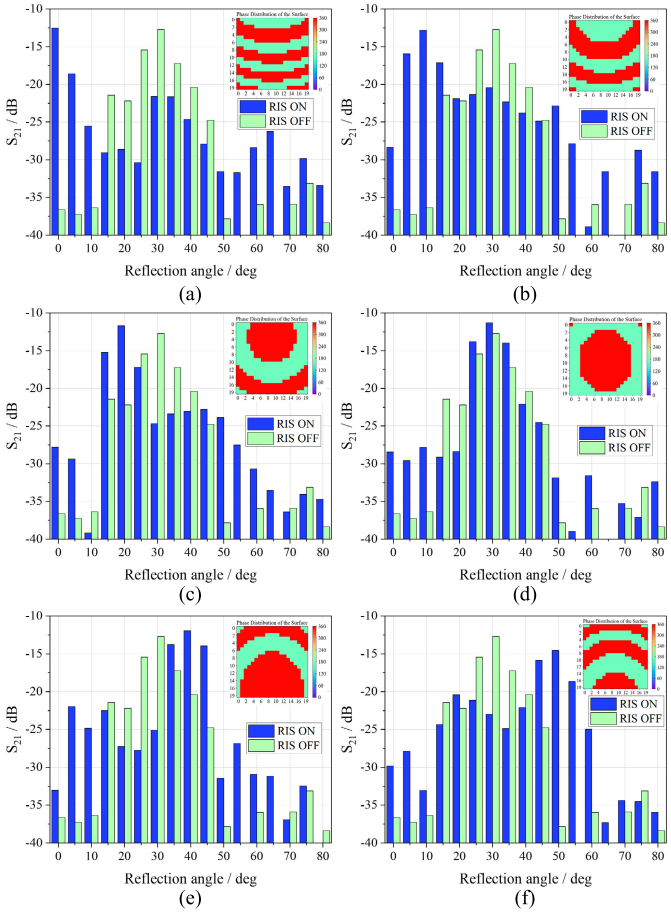

Fig. 20. Measured S_{21} between the Tx and Rx horns when pattern on and off at different reflected beam directions. (a) 0°. (b) 10°. (c) 20°. (d) 30°. (e) 40°. (f) 50°.

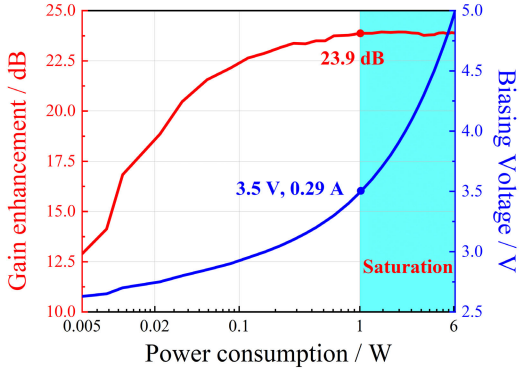

Fig. 21. Measured gain enhancement effect changed with different RIS dc power consumption.

pattern configuration. The measured S_{21} parameters between two horns for the desired beam reflection direction from 0° to 50° are −12.5, −12.8, −11.7, −11.3, −11.9, and −14.5 dB. Moreover, the SLL values for reflection angles from 0° to 50° are 9.1, 7.6, 11.3, 16.5, 12.9, and 5.8 dB. Thus, the proposed RIS design could demonstrate a beam steering capability of up to 50°.

Power consumption is one crucial evaluation aspect for an RIS because the p-i-n diodes require biasing voltage and current. Therefore, we have characterized the power consumption of our design and plotted it (in logarithmic coordinates) along with the gain enhancement in Fig. 21. Here, the measurement

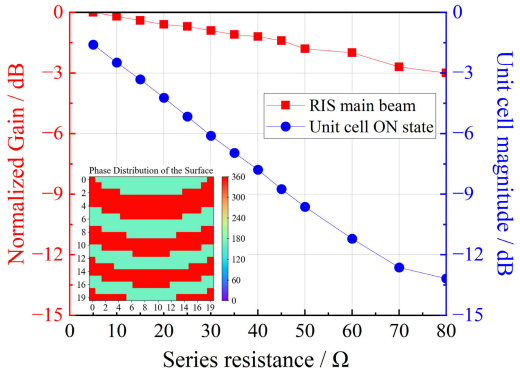

Fig. 22. Calculated RIS normalized gain with different series resistances of the ON state unit cells.

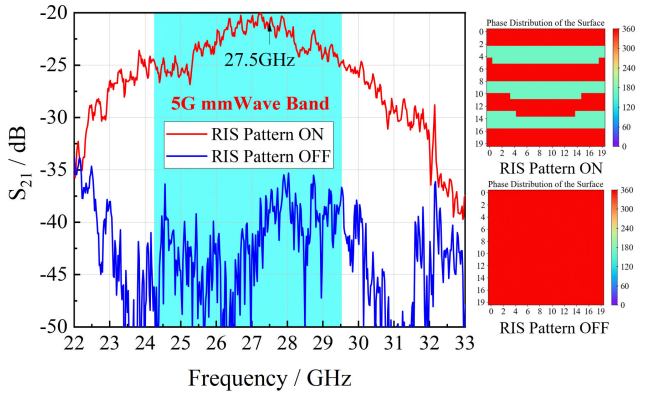

Fig. 23. Measured S_{21} between Tx and Rx horns when turning on/off the RIS pattern in the near-field with Tx-RIS distance of 75 cm and Rx-RIS distance of 35 cm.

parameters are the same as those in the experiment in Fig. 15, where the Tx-RIS distance is 25 cm with a −30° incident angle, and the RIS-Rx distance is 35 cm with a 0° reflection with the operational frequency at 27.5 GHz. It can be observed from Fig. 21 that when the biasing voltage is 3.5 V and the total current is 0.29 A, with a power consumption of 1 W, the proposed RIS design is saturated. Though this 1 W dc power consumption is below the recommended biasing condition from the p-i-n diode datasheet, it is sufficient for the best gain enhancement from this RIS design. With further increase in bias (5 V; 1.23 A), and power consumption (6.2 W), the RIS cannot provide more gain enhancement. Therefore, it can be concluded that the decent required power supply for the proposed RIS is 1 W. Another observation from Fig. 21 is that the power consumption can be further reduced to 0.12 W if the operating conditions are chosen to be 2.95 V and 0.04 A. The proposed RIS could still provide 22.6 dB gain enhancement, which is only 1.3 dB less than the peak gain but with approximately 90% power consumption reduction.

When the biasing current of the p-i-n diode becomes lower, the series resistance gets larger for the unit cells at ON states. To validate the experimental results, the calculated normalized RIS main beam gain with different series resistances of p-i-n diode at ON state has been shown in Fig. 22. Here, the pattern has 194 ON states and 206 OFF states, which is a typical representation for the RIS patterns (half unit cells are at ON states while half unit cells are off). The calculated results show that even with a large series resistance for unit cells at ON states, the RIS main beam can still provide a robust and decent gain enhancement. In other words, by deploying a slightly lower biasing current for p-i-n diodes at ON states, the RIS can generate almost the same level of gain enhancement, which is generally matched with our measured results. The reason is that even if half of the overall unit cells at ON states have a weak reflection, the remaining half unit cells at OFF states are not affected by the biasing current, which has a strong reflection magnitude (−0.5 dB).

Different from reflectarray antennas, the feeding source away from the reconfigurable surface is constant, and the incident beam from a base station or users imping on the RIS could with arbitrary distance. Therefore, additional experiments with different Tx-RIS distances are significant for evaluating the RIS performance. In previous measurements, the Tx-RIS distance is fixed at 25 cm, which belongs to the near-field test. To further prove the RIS near-field gain enhancement function, another random Tx-RIS distance is selected and measured within the near-field region (75 cm in this experiment). Hence, in this experiment, the Tx horn is moved to a distance of 75 cm to represent a base station or user with a particular near-field distance, whereas the Rx horn is kept 35 cm from the RIS to maintain a relatively high received signal power level. The measurement setup has the same configuration as the aforementioned test in that the incident wave angle is 30°, and the desired reflection beam direction is 0°, which is achieved by controlling the RIS pattern [see Fig. 17(a)].

The measured transmission between the Tx and Rx horns, when the RIS pattern is on or off, is depicted in Fig. 23. The signal is enhanced substantially, and an average of 19.6 dB (from −42.6 to −23 dB) is obtained over the entire n257 and n258 bands. Although the signal enhancement has a 5.1 dB reduction compared with the previous test, it is reasonable due to the higher path loss and less effective received area of the RIS compared with the horn placed in a closer distance within the near-field (lower spillover efficiency). Nevertheless, both these two experiments proved that the proposed RIS design could realize decent signal enhancement with a large bandwidth over the entire interested 5G bands for base station or user with various incident distances.

The above measurements are near-field tests, where the Tx horn is 25 and 75 cm away from the RIS and the incident wave impinging on the RIS is a spherical wave. To validate the proposed RIS performance in the far-field region, it is necessary to increase the Tx distance and ensure plane wave illumination, which requires a phase error of less than 22.5 degrees across the RIS aperture [30]. The field generated from a horn antenna can be modeled as a spherical wave starting from the phase center of the horn [30]. Therefore, the far-field measurement distance should be at least $2D^2/\lambda = 2.2$ m, where D is the RIS aperture size and λ is the wavelength at 27.5 GHz.

In this experiment, the Tx horn is located approximately 2.6 m 30° away from the RIS while the RIS-Rx distance is around 2.2m, which can ensure that the RIS is illuminated by a plane wave. The measurement setup is shown in Fig. 24. The Tx horn is connected to the Keysight VXG M9384B

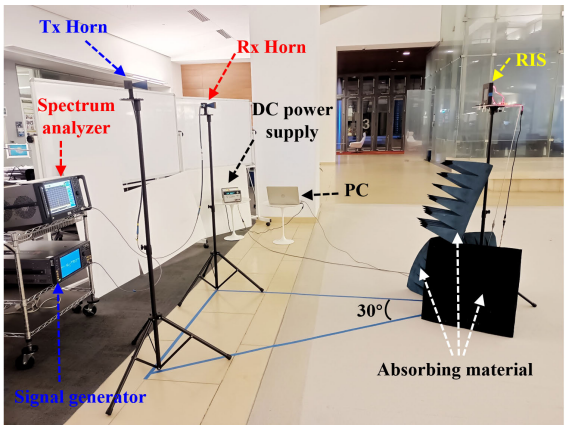

Fig. 24. Measurement setup for the far-field characterization of the proposed RIS.

signal generator to transmit a single tone continuous wave. The Rx horn is connected to the Keysight UXA N9040B signal analyzer with 10 kHz Intermediate Frequency (IF) bandwidth. The power supply provides the dc voltage and the currents required to bias the RIS p-i-n switches, and the PC uploads the commands to the RIS controller to configure the array pattern. Three identical tripods, with the same heights of 1.4 m, are utilized to hold the RIS, Tx, and Rx horns. The entire setup is in a regular indoor environment with open space. Some pieces of absorbers are placed in the surroundings of the RIS tripod to reduce the interference and multiple reflections from the environment.

Fig. 25 demonstrates the received ON/OFF power spectrums in the far-field with 2.6 m Tx-RIS distance and 2.2 m RIS-Rx distance from 22.5 to 29.5 GHz. Here, the input power from the signal generator is set as 0 dBm. The sample bandwidth is 100 MHz with 1001 points. The measured results show that the RIS pattern has become "strip type" when working at the far-field region, which differs from the "spherical type" pattern shape in the near field. When the RIS pattern is turned on, compared with the OFF state, the desired beam (0° reflection) has gain enhancements of 18.6, 18.8, 22.2, 16.4, 16.4, 20.3, 22.5, 16.3 dB for operation frequencies of 22.5, . . . , 29.5 GHz, respectively. In conclusion, an average gain enhancement of 18.9 dB has been obtained across the operation bandwidth when the RIS is illuminated with a plane wave. The specific received power level can be calculated through the radar range equation [30]

$$P_{Rx} = P_{Tx}(1-|S_{11}|)^2(1-|S_{22}|)^2 \times \left(\frac{\lambda}{4\pi d_{Tx-RIS} d_{RIS-Rx}}\right)^2 \frac{G_{Tx}G_{Rx}}{4\pi}\sigma_{RIS}. \quad (3)$$

The P_{Rx} is the received power from the Rx horn, P_{Tx} is the transmitted power at the Tx horn, and $|S_{11}|$ and $|S_{22}|$ are the return loss of the Tx and Rx horns, respectively. λ is the free-space wavelength, $d_{\mathrm{Tx\text{-}RIS}}$ denotes the distance between the Tx horn and RIS, while $d_{\mathrm{RIS\text{-}Rx}}$ represents the RIS and Rx horn distance. G_{Tx} and G_{Rx} are the gains for the Tx and Rx horns, respectively. σ_{RIS} is the radar cross section (RCS) of the RIS, which can be calculated through the geometric cross-sectional area, reflectivity, and RIS directivity [31], [11]. It has been demonstrated that the array factor can describe the directivity

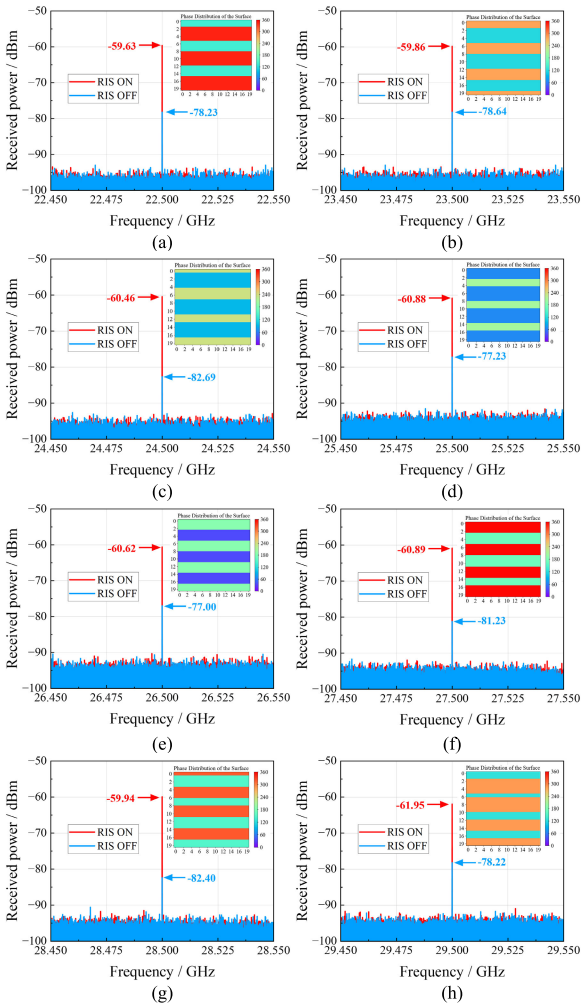

Fig. 25. Measured received power when turning on/off the RIS pattern in the far-field with Tx-RIS distance of 2.6 m and RIS-Rx distance of 2.2 m at different operation frequencies. (a) 22.5 GHz. (b) 23.5 GHz. (c) 24.5 GHz. (d) 25.5 GHz. (e) 26.5 GHz. (f) 27.5 GHz. (g) 28.5 GHz. (h) 29.5 GHz.

of the RIS well when the unit element q factor is 1 [32]. It should be pointed out that there exists a 10 dB attenuation from the spectrum analyzer. In the far-field measurement, the corresponding parameters are as follows: $P_{\mathrm{Tx}} = 0$ dBm; $S_{11} = S_{22} = -15 \sim -20$ dB; $d_{\mathrm{Tx\text{-}RIS}} = 2.6$ m; $d_{\mathrm{RIS\text{-}Rx}} = 2.2$ m; $G_{\mathrm{Tx}} = G_{\mathrm{Rx}} = 20$ dBi; the calculated RIS directivity is 24.6 dB; the RIS aperture size is $7.1\lambda \times 7.1\lambda$; the incident angle is 30°. Therefore, the theoretical received power for the ideal RIS can be calculated to be $P_{\mathrm{Rx}} = -55.9$ dBm, while the measured received power is -60.9 dBm. Hence, around 5 dB of power is dissipated due to various losses and practical imperfections of the RIS, including 1-bit phase quantization loss, conductor loss, dielectric loss, p-i-n diodes loss, and so on. The RIS loss characterization in the far-field can also be determined by comparing RIS with a metallic sheet that has the same size as the RIS aperture. It provides a measurement method for characterizing RIS losses [17]. In this work, we also compare the received power level of RIS with a metallic sheet, and a 4.2 dB received power difference is obtained, which generally matches the calculated loss value of 5 dB. Meanwhile, it can be seen that the received power level is robust when turning on the RIS pattern within the whole bandwidth, which varies

TABLE I
PERFORMANCE COMPARISON WITH PREVIOUS RIS DESIGNS

Ref.	Freq. (GHz)	Unit BW (%)	Size (λ^2)	Gain BW (%)	Signal enhancement (dB)		Consumed power (W)
					Near field	Far field	
[11]	5.2	3.1	10.4× 10.4	<5.8	NA	~15	NA
[13]	3.15	14	3×3	<14	NA	NA	NA
[14]	5.8	8.7	15.5× 6.1	<8.7	NA	27	1
[17]	28.5	7.0	9.5× 9.5	7.3	~30	~25	8
This work	27.5	29.3	7.1× 7.1	26.9	24.7	18.9	1

from −62 to −59.6 dBm. Based on all the above-conducted measurements, it can be concluded that the proposed RIS design provides promising gain enhancement for both the near field and the far-field over a wide bandwidth (covering the 5G bands). Lastly, it should be pointed out that the phase quantization will result in quantization lobes in the far-field for the RIS design. Some algorithm improvement techniques can be utilized, such as the genetic algorithm, particle swarm optimization algorithm, to reduce the phase quantization effect, which can be investigated in future work.

To compare the proposed work with previous practical RIS designs, the features of this work are summarized in Table I. Most RISs have a narrow bandwidth of less than 14% [11], [13], [14], [17]. As discussed, the previously published literature has primarily focused on the sub-6 band [11], [13], [14]. The work proposed in [17] aimed at a 5G mm-wave design, but the bandwidth is 7.3%, which cannot cover the entire 5G n257 and n258 bandwidths. Moreover, [17] did not perform an actual far-field measurement that the RIS with an aperture size of $10\lambda \times 10\lambda$ should have at least a Tx-RIS distance of approximately 4 m to ensure the plane wave illumination on the RIS aperture. In this work, the proposed design with a measured 26.9% bandwidth is the highest for the RIS operating at the 5G mm-wave band.

V. CONCLUSION

In this work, we designed a novel wideband RIS operating in the 5G mm-waveband, and the unit cell has a bandwidth of 29.3% (22.7 to 30.5 GHz). Wideband performance is realized by the two high-order resonances with 2.5 and 3.5 f operation frequencies, which demonstrates a decent unit cell performance with incident angular stability of ±30°. A final RIS design with a 20 × 20 array configuration is fabricated and measured with a total size of $7.1\lambda \times 7.1\lambda$ revealing a 3 dB gain bandwidth of 26.9% (covering the whole 5G mm-wave n257 and n258 bands). The design can scan a reflection beam of up to 50°. Therefore, the proposed RIS design with wideband reflection characteristics is suitable for the 5G mm-wave communication system.

REFERENCES

[1] T. S. Rappaport, Y. Xing, G. R. MacCartney, A. F. Molisch, E. Mellios, and J. Zhang, "Overview of millimeter wave communications for fifth-generation (5G) wireless networks—With a focus on propagation models," *IEEE Trans. Antennas Propag.*, vol. 65, no. 12, pp. 6213–6230, Dec. 2017.

[2] K. Klionovski, M. S. Sharawi, and A. Shamim, "A dual-polarization-switched beam patch antenna array for millimeter-wave applications," *IEEE Trans. Antennas Propag.*, vol. 67, no. 5, pp. 3510–3515, May 2019.

[3] W. Hong, K.-H. Baek, and S. Ko, "Millimeter-wave 5G antennas for smartphones: Overview and experimental demonstration," *IEEE Trans. Antennas Propag.*, vol. 65, no. 12, pp. 6250–6261, Dec. 2017, doi: 10.1109/TAP.2017.2740963.

[4] P. Mei, S. Zhang, and G. F. Pedersen, "A low-cost, high-efficiency and full-metal reflectarray antenna with mechanically 2-D beam-steerable capabilities for 5G applications," *IEEE Trans. Antennas Propag.*, vol. 68, no. 10, pp. 6997–7006, Oct. 2020.

[5] K. Klionovski, H. Liao, S. E. Bankov, Z. Akhter, and A. Shamim, "A planar SIW-based mm-wave frequency-scanning slot antenna array with no scan blindness at normal," *IEEE Trans. Antennas Propag.*, vol. 71, no. 1, pp. 563–569, Jan. 2023.

[6] L. Dai et al., "Reconfigurable intelligent surface-based wireless communications: Antenna design, prototyping, and experimental results," *IEEE Access*, vol. 8, pp. 45913–45923, 2020.

[7] C. Huang, A. Zappone, G. C. Alexandropoulos, M. Debbah, and C. Yuen, "Reconfigurable intelligent surfaces for energy efficiency in wireless communication," *IEEE Trans. Wireless Commun.*, vol. 18, no. 8, pp. 4157–4170, Aug. 2019.

[8] E. Basar, "Reconfigurable intelligent surface-based index modulation: A new beyond MIMO paradigm for 6G," *IEEE Trans. Commun.*, vol. 68, no. 5, pp. 3187–3196, May 2020.

[9] Q. Wu and R. Zhang, "Beamforming optimization for wireless network aided by intelligent reflecting surface with discrete phase shifts," *IEEE Trans. Commun.*, vol. 68, no. 3, pp. 1838–1851, Mar. 2020.

[10] A. Zappone, M. Di Renzo, and M. Debbah, "Wireless networks design in the era of deep learning: Model-based, AI-based, or both?" *IEEE Trans. Commun.*, vol. 67, no. 10, pp. 7331–7376, Oct. 2019.

[11] A. Sayanskiy et al., "A 2D-programmable and scalable reconfigurable intelligent surface remotely controlled via digital infrared code," *IEEE Trans. Antennas Propag.*, vol. 71, no. 1, pp. 570–580, Jan. 2023.

[12] L. Wu et al., "A wideband amplifying reconfigurable intelligent surface," *IEEE Trans. Antennas Propag.*, vol. 70, no. 11, pp. 10623–10631, Nov. 2022.

[13] J. C. Liang et al., "An angle-insensitive 3-bit reconfigurable intelligent surface," *IEEE Trans. Antennas Propag.*, vol. 70, no. 10, pp. 8798–8808, Oct. 2022.

[14] X. Pei et al., "RIS-aided wireless communications: Prototyping, adaptive beamforming, and indoor/outdoor field trials," *IEEE Trans. Commun.*, vol. 69, no. 12, pp. 8627–8640, Dec. 2021.

[15] X. Cao, Q. Chen, T. Tanaka, M. Kozai, and H. Minami, "A 1-bit time-modulated reflectarray for reconfigurable-intelligent-surface applications," *IEEE Trans. Antennas Propag.*, vol. 71, no. 3, pp. 2396–2408, Mar. 2023.

[16] Z. Zhang et al., "Macromodeling of reconfigurable intelligent surface based on microwave network theory," *IEEE Trans. Antennas Propag.*, vol. 70, no. 10, pp. 8707–8717, Oct. 2022.

[17] J.-B. Gros, V. Popov, M. A. Odit, V. Lenets, and G. Lerosey, "A reconfigurable intelligent surface at mmWave based on a binary phase tunable metasurface," *IEEE Open J. Commun. Soc.*, vol. 2, pp. 1055–1064, 2021.

[18] A. S. Shekhawat, B. G. Kashyap, P. C. Theofanopoulos, A. P. S. Sengar, and G. C. Trichopoulos, "A compact unit-cell design for mmWave reconfigurable intelligent surfaces," in *Proc. United States Nat. Committee URSI Nat. Radio Sci. Meeting (USNC-URSI NRSM)*, Jan. 2022, pp. 84–85.

[19] A. S. Shekhawat, B. G. Kashyap, B. Tjahjadi, and G. C. Trichopoulos, "Beamforming characterization of a mmWave single-bit reflective metasurface," in *Proc. IEEE Int. Symp. Antennas Propag. USNC-URSI Radio Sci. Meeting (AP-S/URSI)*, Jul. 2022, pp. 1608–1609.

[20] J. Rains, J. U. R. Kazim, A. Tukmanov, L. Zhang, Q. H. Abbasi, and M. Imran, "Varactor-based reconfigurable intelligent surface with dual linear polarisation at K-band," in *Proc. IEEE Int. Symp. Antennas Propag. USNC-URSI Radio Sci. Meeting*, Jul. G. W. Stimson, *Introduction to Airborne Radar*, 2nd ed. Mendham, NJ, USA: Science, 1998, ch. 37-39.2022, pp. 673–674.

[21] H. Yang et al., "A 1-bit 10 × 10 reconfigurable reflectarray antenna: Design, optimization, and experiment," *IEEE Trans. Antennas Propag.*, vol. 64, no. 6, pp. 2246–2254, Jun. 2016.

[22] X. Pan, F. Yang, S. Xu, and M. Li, "A 10 240-element reconfigurable reflectarray with fast steerable monopulse patterns," *IEEE Trans. Antennas Propag.*, vol. 69, no. 1, pp. 173–181, Jan. 2021.

[23] F. Wu, R. Lu, J. Wang, Z. H. Jiang, W. Hong, and K.-M. Luk, "A circularly polarized 1 bit electronically reconfigurable reflectarray based on electromagnetic element rotation," *IEEE Trans. Antennas Propag.*, vol. 69, no. 9, pp. 5585–5595, Sep. 2021.

[24] H. Luyen, Z. Zhang, J. H. Booske, and N. Behdad, "Wideband, beam-steerable reflectarray antennas exploiting electronically reconfigurable polarization-rotating phase shifters," *IEEE Trans. Antennas Propag.*, vol. 70, no. 6, pp. 4414–4425, Jun. 2022.

[25] J. Ethier, M. R. Chaharmir, and J. Shaker, "Loss reduction in reflectarray designs using sub-wavelength coupled-resonant elements," *IEEE Trans. Antennas Propag.*, vol. 60, no. 11, pp. 5456–5459, Nov. 2012.

[26] P. Nayeri, F. Yang, and A. Z. Elsherbeni, *Reflectarray Antennas: Theory, Designs, and Applications*. Hoboken, NJ, USA: Wiley, 2018.

[27] S. M. A. Momeni Hasan Abadi, K. Ghaemi, and N. Behdad, "Ultra-wideband, true-time-delay reflectarray antennas using ground-plane-backed, miniaturized-element frequency selective surfaces," *IEEE Trans. Antennas Propag.*, vol. 63, no. 2, pp. 534–542, Feb. 2015.

[28] Y. Li, M. E. Bialkowski, and A. M. Abbosh, "Single layer reflectarray with circular rings and open-circuited stubs for wideband operation," *IEEE Trans. Antennas Propag.*, vol. 60, no. 9, pp. 4183–4189, Sep. 2012.

[29] A. Al-Zayed, R. R. Swisher, F. Lecuyer, A. C. Guyette, Q. Sun, and M. P. De Lisio, "Reduction of substrate-mode effects in power-combining arrays," *IEEE Trans. Microw. Theory Techn.*, vol. 49, no. 6, pp. 1067–1072, Jun. 2001.

[30] C. A. Balanis, *Antenna Theory: Analysis and Design*. Hoboken, NJ, USA: Wiley, 2005.

[31] G. W. Stimson, *Introduction to Airborne Radar*, 2nd ed. Mendham, NJ, USA: Science, 1998, ch. 37-39.

[32] A. Yu, F. Yang, A. Z. Elsherbeni, J. Huang, and Y. Rahmat-Samii, "Aperture efficiency analysis of reflectarray antennas," *Microw. Opt. Technol. Lett.*, vol. 52, no. 2, pp. 364–372, Feb. 2010.

Ruiqi Wang received the B.S. degree in electronic engineering from the University of Electric Science and Technology of China (UESTC), Chengdu, China, in 2021, and the M.S. degree in electrical and computer engineering from the King Abdullah University of Science and Technology (KAUST), Thuwal, Saudi Arabia, in 2022, where he is currently pursuing the Ph.D. degree.

His current research interests include antenna radiation pattern synthesis and reconfigurable intelligent surfaces.

Yiming Yang (Graduate Student Member, IEEE) was born in Shandong, China, in 1997. He received the B.S. degree from the University of Electric Science and Technology of China (UESTC), Chengdu, China, in 2020, and the M.S. degree from the King Abdullah University of Science and Technology (KAUST), Thuwal, Saudi Arabia, in 2021.

His research interests include reconfigurable intelligent surfaces, frequency-selective surfaces, microwave measurement, and additive manufacturing of antennas and radio frequency (RF) circuits.

Mr. Yang was a finalist and received the first prize in AP-S Student Design Contest in 2020 and 2022, respectively.

Behrooz Makki (Senior Member, IEEE) received the Ph.D. degree in communication engineering from the Chalmers University of Technology, Gothenburg, Sweden, in 2013.

He was a Post-Doctoral Researcher at the Chalmers University of Technology from 2013 to 2017. He is currently working as a Senior Researcher with Ericsson Research, Gothenburg. He has coauthored more than 70 journal articles, more than 50 conference papers, and more than 100 patent applications. His current research interests include integrated access and backhaul, millimeter wave communications, intelligent reflecting surfaces, and free-space optical communication.

Dr. Makki was an Editor of IEEE WIRELESS COMMUNICATIONS LETTERS, IEEE TRANSACTIONS ON COMMUNICATIONS, and IEEE TRANSACTIONS ON WIRELESS COMMUNICATIONS, and also a Senior Editor in IEEE COMMUNICATIONS LETTERS.

Atif Shamim (Fellow, IEEE) received the M.S. and Ph.D. degrees in electrical engineering from Carleton University, Ottawa, ON, Canada, in 2004 and 2009, respectively.

He was an NSERC Alexander Graham Bell Graduate Scholar at Carleton University from 2007 to 2009 and an NSERC Postdoctoral Fellow from 2009 to 2010 at the Royal Military College Canada, Kingston, ON, Canada, and the King Abdullah University of Science and Technology (KAUST), Thuwal, Saudi Arabia. In August 2010, he joined the Electrical Engineering Program, KAUST, where he is currently a Professor and Principal investigator of the IMPACT Laboratory. He was an invited Researcher with the VTT Micro-Modules Research Center, Oulu, Finland, in 2006. He is an author/coauthor of 300 international publications, an inventor on more than 40 patents, and has given close to 100 invited talks at various international forums. His research interests include innovative antenna designs and their integration strategies with circuits and sensors for flexible and wearable wireless sensing systems through a combination of CMOS and additive manufacturing technologies.

Prof. Shamim was a recipient of best paper awards in IEEE Instrumentation and Measurement Society (IMS) 2016, IEEE Middle East Conference on Antennas and Propagation (MECAP) 2016, IEEE European Wireless Technology Conference (EuWiT) 2008; first prize in the IEEE IMS 2019 3MT Competition and finalist/honorable mention prizes in IEEE Antennas and Propagation Society (APS) Design Competition 2020, IEEE APS 2005, IEEE IMS 2014, IEEE IMS 2017 (3MT competition); and R. W. P. King IEEE Award for journal papers in IEEE TRANSACTIONS ON ANTENNAS AND PROPAGATION 2017 and 2020. He was a recipient of the Ottawa Centre of Research Innovation (OCRI) Researcher of the Year Award in Canada, in 2008. His work on wireless dosimeter won the ITAC SMC Award at Canadian Microelectronics TEXPO in 2007. He also was a recipient of numerous business-related awards, including 1st Prize in Canada's National Business Plan Competition and was awarded OCRI Entrepreneur of the Year Award in 2010 and the Kings Prize for the best innovation of the year in 2018 for his work on sensors for the oil industry. He is a member of the IEEE APS Measurements Committee and the IEEE MTT Microwave Control Techniques Committee, founded the first IEEE AP/MTT chapter in Saudi Arabia in 2013, and served on the Editorial Board of IEEE TRANSACTIONS ON ANTENNAS AND PROPAGATION from 2013 to 2019, and as the Guest Editor for Special Issue of IEEE ANTENNAS AND WIRELESS PROPAGATION LETTERS (AWPL) in 2019. He is currently an Associate Editor for IEEE JOURNAL OF ELECTROMAGNETICS, RF AND MICROWAVES IN MEDICINE AND BIOLOGY. He has been selected as the Distinguished Lecturer for AP-S from 2022 to 2024.